Adaptation of f-wave finite volume methods to the two-layer shallow-water equations in a moving vessel with a rigid-lid

by H. Alemi Ardakani [1], T.J. Bridges & M.R. Turner

Department of Mathematics, University of Surrey, Guildford, Surrey GU2 7XH, England

Abstract. A numerical method is proposed to solve the two-layer inviscid, incompressible and immiscible 1D shallow-water equations in a moving vessel with a *rigid-lid* with different boundary conditions based on the high-resolution f-wave finite volume methods due to Bale, LeVeque, Mitran and Rossmanith [7] (2002, SIAM J. Sci. Comput. **24**). The method splits the jump in the fluxes and source terms including the *pressure gradient* at the rigid-lid into waves propagating away from each grid cell interface. For the influx-efflux boundary conditions the time dependent source terms are handled via a fractional step approach. In the linear case the numerical solutions are validated by comparison with the exact analytical solutions. Numerical solutions presented for the nonlinear case include shallow-water sloshing waves due to prescribed surge motion of the vessel.

1 Introduction

Multiple layers with differing density are widely used as simplified models for stratified flows, and are particularly useful when the density stratification is sharp. The interest here is in two-layer flow in shallow water where the flow is bounded above by a rigid lid. The main difficulty is that the rigid lid requires a constraint, which is enforced by including a pressure field in the equations. Our motivation is modelling ocean wave energy harvesters which bring in additional difficulties: the vessel is moving, there is mass flux into and out of the vessel, and wetting and drying may occur. In this paper we consider the two-layer shallow water model with a rigid lid with both fixed boundaries and influx-efflux boundaries, and the simplest case of vessel motion (surge), whereas wetting-drying is left for future work. An introduction to shallow water multi-layer models is given in the book of Baines [6]. There has been a vast number of studies of two layer models, too numerous to mention here, but papers that have influenced the strategy here are [5, 7, 8, 9, 10, 12, 13, 14, 15, 16, 18, 19, 20, 21, 24, 25, 26, 27, 28, 29, 30].

The ocean wave energy converter (WEC) proposed by Offshore Wave Energy Ltd (OWEL),

[1]Corresponding author: email: h.alemiardakani@surrey.ac.uk; Phone: +44 (0)1483 689643; Fax: +44 (0)1483 686071.

a schematic of which can be found on the website [1], is a floating rectangular device, open at one end to allow waves in. Once they are trapped, the waves undergo interior fluid sloshing. A rise in the wave height is induced within the duct. The wave then creates a seal with the rigid lid resulting in a moving trapped pocket of air ahead of the wave front which drives the power take off. The strategy is to use the two-layer inviscid, incompressible and immiscible shallow-water equations as a starting point in studying the dynamics of the fluid flows in these floating offshore structures.

A class of high resolution wave-propagation finite volume methods are developed in [22] for multidimensional hyperbolic systems. These methods are based on solving Riemann problems for waves that define both first order updates to cell averages and also second order corrections which can be modified by limiter functions to obtain high resolution numerical solutions. The wave-propagation algorithms are modified in [7] for conservation laws and balance laws with spatially varying flux functions and called f-wave-propagation methods. The main novel feature of the modified algorithms is to solve the Riemann problems by decomposition of the jump in the flux functions into waves propagating out from each grid cell interface instead of decomposition of the jump in cell averages. In [14, 15] a class of augmented approximate Riemann solvers is developed for the single layer shallow water equations in the presence of a variable bottom surface using the f-wave-propagation algorithm. The solver is based on a decomposition of an augmented solution vector including the depth, momentum, momentum flux and the bottom surface. This solver is well-balanced, maintains depth non-negativity and extends to Riemann problems with an initial dry state. In [26, 27] the f-wave-propagation finite volume method is used to develop solvers for the multilayer shallow water equations in one and two dimensions. The proposed approximate Riemann solvers also handle dry states in the system where the bottom layer depth becomes zero. In [19] the two-layer shallow water system is studied using the f-wave methods. It is discussed that the two-layer system is conditionally hyperbolic because of the coupling terms between the layers. These terms may cause the eigenvalues to become imaginary. In [18] the f-wave method is used to solve the wave propagation problems generated by submarine landslides. Also several types of the Boussinesq equations are reviewed and implemented with a hybrid of high-resolution finite volume and finite difference methods. In [25] a numerical scheme for solving the shallow water equations with local bed efflux/influx is developed based on a modified wave propagation algorithm.

In this paper we are interested in the numerical study of the two-layer shallow-water flows with a rigid-lid with f-wave-propagation high resolution finite volume methods. To our knowledge this is the first paper which uses the f-wave methods to solve the two-layer shallow water system with the *rigid-lid pressure gradient*, and time-dependent forcing for two-layer shallow-water sloshing.

The two-layer shallow-water system with a rigid-lid and horizontal surge forcing can be derived by integrating the Euler equations in the vertical coordinate direction. The starting

point for the paper is the governing 1D equations in the form

$$\begin{aligned}
(\rho_1 h_1)_t + (\rho_1 h_1 u_1)_x &= 0\,, \\
(\rho_1 h_1 u_1)_t + \left(\rho_1 h_1 u_1^2 + \tfrac{1}{2}\rho_1 g h_1^2\right)_x &= -\rho_1 g h_1 h_{2x} - h_1 p_x - \rho_1 h_1 \ddot{q}\,, \\
(\rho_2 h_2)_t + (\rho_2 h_2 u_2)_x &= 0\,, \\
(\rho_2 h_2 u_2)_t + \left(\rho_2 h_2 u_2^2 + \tfrac{1}{2}\rho_2 g h_2^2\right)_x &= -\rho_1 g h_2 h_{1x} - h_2 p_x - \rho_2 h_2 \ddot{q}\,, \\
h_1(x,t) + h_2(x,t) &= d\,,
\end{aligned} \tag{1.1}$$

where h_1, u_1 and ρ_1 denote the depth, velocity and density of the upper layer, and h_2, u_2 and ρ_2 correspond to the lower layer. The variable p is the pressure at the rigid-lid, and g is the gravity constant. The function $q(t)$ is the prescribed surge forcing which will be included in §6. The last equation in (1.1) is the rigid-lid constraint with d a given positive constant representing the height of the vessel. The first and third equations in (1.1) are the conservation of mass, and the second and fourth equations are the conservation of momentum for each layer.

Another form of the two-layer shallow water system (1.1) is obtained by replacing the fourth equation of (1.1) by

$$(\rho_2 h_2 u_2)_t + \left(\rho_2 h_2 u_2^2 + \tfrac{1}{2}\rho_2 g h_2^2 + \rho_1 g h_1 h_2\right)_x = \rho_1 g h_1 h_{2x} - h_2 p_x - \rho_2 h_2 \ddot{q}\,. \tag{1.2}$$

The form of the fourth equation is chosen so that the non-conservative coupling terms in each layer become symmetric [5, 27]. The symmetry in the non-conservative products has the benefit that the transfer of momentum due to these coupling terms moves directly between the layers which is advantageous in numerical integration [27]. A schematic of the two-layer shallow-water system with a rigid-lid is shown in Figure 1.

In solving the two-layer shallow-water system numerically several difficulties arise. First, because the two-layer 1D shallow-water equations are in non-conservative form, the system of equations is conditionally hyperbolic. Secondly, an explicit expression cannot be found for the eigenvalues of the two layer system which is inconvenient for Riemann solution based numerical schemes [19, 5]. Thirdly, a numerical scheme is required to be well-balanced with source terms since the quasi-linear two-layer shallow-water system is non-conservative [19]. Fourthly, the non-conservative products are not well-defined for discontinuous solutions which can lead to several notions of weak solutions [9]. In practice, there is a lack of a Rankine-Hugoniot condition in order to define jump relations at a discontinuity [9]. The disadvantage of using the system (1.2) rather than the system (1.1) is that the flux Jacobian of (1.2) gives eigenvalues and eigenvectors which would be identical to two uncoupled shallow-water equation systems [27, 12]. It is shown in [12] that the approach of using a splitting of the layers would be unstable [27] unless suitable corrections are used [9, 27]. Since the wave speeds predicted by the eigenstructure of the system (1.2) do not take into account the coupling between the layers, the eigenstructure of this system is not desirable for methods that depend on this information to construct a Riemann solution [27]. So the strategy is to use the two-layer shallow water system (1.1) to determine the required eigenstructure for the f-wave finite volume analysis, and use the system (1.2) to calculate the jump in the fluxes.

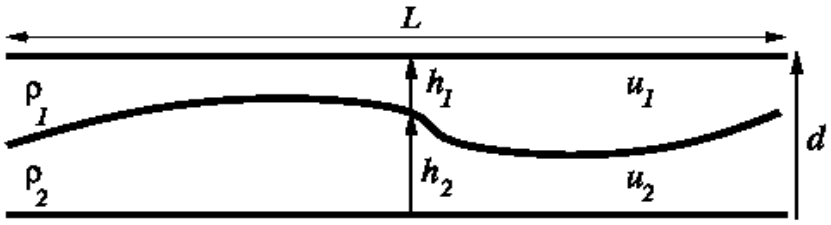

Figure 1: Schematic of two-layer fluids bounded by horizontal top and bottom impermeable walls.

The paper starts by pre-conditioning the governing equations (1.1) [26, 27] for numerics in §2. The essential details of the f-wave finite volume method are discussed in §3. The exact linear solution for the two-layer shallow water system with a rigid-lid is recorded in §4. For validation, a linear f-wave finite volume solver is developed in §5.1 in order to compare the numerical results with the exact linear solutions with rigid wall boundary conditions. F-wave finite volume solvers are developed for the full nonlinear hyperbolic systems with rigid walls in §5.2. In §6 some results are presented for two-layer shallow water waves sloshing inside a container with a rigid-lid and under a prescribed surge forcing. In §7.1 a fractional step approach together with the f-wave algorithm is used to solve the linear two-layer shallow-water system with influx-efflux boundary conditions. The numerical solutions are compared with the exact solutions in §4. F-wave finite volume solvers are developed for the fully nonlinear hyperbolic systems with influx-efflux boundary conditions in §7.2. Finally the paper ends with some concluding remarks in §8.

2 Pre-conditioning the equations for numerics

The two-layer shallow water system (1.1) can be written in the following balance law form

$$\mathsf{q}_t + f(\mathsf{q})_x = \Psi(\mathsf{q}) \,, \tag{2.1}$$

where

$$\mathsf{q}(x,t) = \begin{bmatrix} \rho_1 h_1 \\ \rho_1 h_1 u_1 \\ \rho_2 h_2 \\ \rho_2 h_2 u_2 \end{bmatrix}, f(\mathsf{q}) = \begin{bmatrix} \rho_1 h_1 u_1 \\ \rho_1 h_1 u_1^2 + \frac{1}{2}\rho_1 g h_1^2 \\ \rho_2 h_2 u_2 \\ \rho_2 h_2 u_2^2 + \frac{1}{2}\rho_2 g h_2^2 \end{bmatrix}, \Psi(\mathsf{q}) = \begin{bmatrix} 0 \\ -\rho_1 g h_1 h_{2x} - h_1 p_x - \rho_1 h_1 \ddot{q} \\ 0 \\ -\rho_1 g h_2 h_{1x} - h_2 p_x - \rho_2 h_2 \ddot{q} \end{bmatrix}.$$

This system can be written in *quasi-linear* form as

$$\mathsf{q}_t + A(\mathsf{q})\,\mathsf{q}_x = \widehat{\Psi}(\mathsf{q}) \,, \tag{2.2}$$

where the Jacobian matrix $A(\mathsf{q})$ and the vector of source terms $\widehat{\Psi}(\mathsf{q})$ are

$$A(\mathsf{q}) = \begin{bmatrix} 0 & 1 & 0 & 0 \\ -u_1^2 + g h_1 & 2u_1 & r g h_1 & 0 \\ 0 & 0 & 0 & 1 \\ g h_2 & 0 & -u_2^2 + g h_2 & 2u_2 \end{bmatrix}, \quad \widehat{\Psi}(\mathsf{q}) = \begin{bmatrix} 0 \\ -h_1 p_x - \rho_1 h_1 \ddot{q} \\ 0 \\ -h_2 p_x - \rho_2 h_2 \ddot{q} \end{bmatrix}.$$

The characteristic polynomial of $A(\mathsf{q})$ reads

$$\left((\lambda-u_2)^2-gh_2\right)\left((\lambda-u_1)^2-gh_1\right)-rg^2h_1h_2=0\,, \tag{2.3}$$

where $r=\dfrac{\rho_1}{\rho_2}$. Interesting geometrical interpretations of (2.3) are discussed in [28, 19, 18]. Several approaches have been used to find the eigenvalues of the characteristic equation (2.3). In [21] an explicit expression for the roots of a fourth degree polynomial is used to evaluate the eigenvalues directly. This approach is appealing and it is being tested on the equations for the two-fluid system. However, numerically this direct approach is expensive and difficult to do with precision [27]. Instead different approaches are used to approximate the eigenspace. In [29] a velocity difference expansion method is used to evaluate the eigenvalues. Approximations are based on an expansion about the differences in layer speeds u_1-u_2. Under the assumptions that $|u_1-u_2|$ and $(1-r)$ are very small, first order approximations for the eigenspeeds are

$$\lambda^{\pm}_{\text{ext}}\approx\frac{h_1u_1+h_2u_2}{h_1+h_2}\pm\sqrt{g\,(h_1+h_2)}\,, \tag{2.4}$$

corresponding to wave speeds of surface waves and

$$\lambda^{\pm}_{\text{int}}\approx\frac{h_1u_2+h_2u_1}{h_1+h_2}\pm\sqrt{g'\frac{h_1h_2}{h_1+h_2}\left(1-\frac{(u_1-u_2)^2}{g'\,(h_1+h_2)}\right)}\,, \tag{2.5}$$

where $g'=g\,(1-r)$ is the reduced gravity, corresponding to wave speeds at the internal surface. So it can be concluded that the internal eigenvalues $\lambda^{\pm}_{\text{int}}$ are conditionally real if

$$\frac{(u_1-u_2)^2}{g'\,(h_1+h_2)}<1\,, \tag{2.6}$$

and it is expected when $|u_1-u_2|$ becomes large enough the shear stress grows and leads to the Kelvin-Helmholtz (KH) instability. So this condition is linked to the KH instability of the stratified flows [19, 18]. See [11] for the numerical treatment of the loss of hyperbolicity of the two layer shallow water system, and see [8] for the nonlinear stability analysis of two-layer shallow water equations with a rigid-lid. This approach for the approximation of the eigenvalues is useful only for two-layer shallow fluid flows with densities very close to each other (Boussinesq approximation). In this paper we are interested in two-layer shallow fluid flows within the non-Boussinesq limit. Hence, we adapt the following approach for the approximation of the eigenvalues.

Another approach to approximating the eigenstructure of (1.1) is to use the eigenvalues of the linearized system [27] with the characteristic polynomial

$$\left(\lambda^2-gh_2^0\right)\left(\lambda^2-gh_1^0\right)-rg^2h_1^0h_2^0=0\,, \tag{2.7}$$

where h_1^0 and h_2^0 are the upper layer and lower layer fluid depths at rest, respectively. Assuming that the eigenvectors have the form $\widetilde{\mathrm{x}}=[1,\lambda,\chi,\lambda\chi]^T$, the unknowns λ and χ can be found from $A\widetilde{\mathrm{x}}=\lambda\widetilde{\mathrm{x}}$, A is defined in (4.1),

$$\begin{aligned} gh_1^0\,(1+\chi r) &= \lambda^2\,,\\ gh_2^0\,(1+\chi) &= \lambda^2\chi\,. \end{aligned} \tag{2.8}$$

Now eliminating λ from both equations, a quadratic equation for χ can be found

$$\chi^2 + \frac{1}{r}(1-\beta)\chi - \frac{\beta}{r} = 0\,, \tag{2.9}$$

giving

$$2\chi^{\pm} = -\frac{1}{r}(1-\beta) \pm \frac{1}{r}\sqrt{(1-\beta)^2 + 4\beta r}\,, \tag{2.10}$$

where $\beta = \dfrac{h_2^0}{h_1^0}$. Now λ can be found in terms of either the top or bottom layers,

$$\begin{aligned} \lambda &= \pm\sqrt{gh_1^0}\sqrt{1+\chi r}\,, \\ \lambda &= \pm\sqrt{gh_2^0}\sqrt{\frac{1+\chi}{\chi}}\,, \end{aligned} \tag{2.11}$$

and it is discussed in [27, 19, 18] that the external and internal eigenvalues are

$$\begin{aligned} \lambda^1_{\text{ext}} &= -\sqrt{gh_1^0(1+\chi^+ r)}\,, \quad \lambda^1_{\text{int}} = -\sqrt{gh_1^0(1+\chi^- r)}\,, \\ \lambda^2_{\text{int}} &= \sqrt{gh_1^0(1+\chi^- r)}\,, \quad \lambda^2_{\text{ext}} = \sqrt{gh_1^0(1+\chi^+ r)}\,, \end{aligned} \tag{2.12}$$

with eigenvectors

$$\Lambda = \begin{bmatrix} 1 & 1 & 1 & 1 \\ -\sqrt{gh_1^0(1+\chi^+ r)} & -\sqrt{gh_1^0(1+\chi^- r)} & \sqrt{gh_1^0(1+\chi^- r)} & \sqrt{gh_1^0(1+\chi^+ r)} \\ \chi^+ & \chi^- & \chi^- & \chi^+ \\ -\chi^+\sqrt{gh_1^0(1+\chi^+ r)} & -\chi^-\sqrt{gh_1^0(1+\chi^- r)} & \chi^-\sqrt{gh_1^0(1+\chi^- r)} & \chi^+\sqrt{gh_1^0(1+\chi^+ r)} \end{bmatrix}. \tag{2.13}$$

Since the eigenspace is completely determined by the initial conditions in the linear limit and does not change in time, an alternative to this is to use the full values of β, h_1 and h_2 for the nonlinear equations [26]. This eigenspace is valid for both the two-layer shallow-water systems (1.1) and (1.2) [27]. We use this approach to approximate the eigenstructure of the two-layer shallow water system in this paper.

Another approach in approximating the eigenspace of the nonlinear equations is to use a numerical eigensolver such as LAPACK [27]. In using the f-wave finite volume methods the state at which the quasi-linear matrix $A(\mathsf{q})$ in (2.2) should be evaluated is prescribed. But since the f-wave method is conservative regardless of the linearization used, a simple arithmetic average of the state vector q can be used to evaluate the quasi-linear matrix [26, 27]. A comparison of the different approaches described in this section is given in [27] for the approximation of the eigenspace of the two layer shallow water equations with dry states.

The third approach in approximating the eigenpairs which is used in this paper seems to be cheaper than using a numerical eigensolver such as LAPACK. However a comparison of both approaches for the numerical schemes used in the paper could be an interesting topic for further research.

3 The f-wave-propagation numerical approach

The numerical method used in this paper to implement the linear and nonlinear two layer shallow water equations with a rigid-lid is the high resolution wave propagation finite volume algorithm developed by Bale et al. [7, 23] and used by [15, 27, 18]. This method is briefly discussed here. Interested readers are referred to [7, 23, 14, 24, 15, 26, 27, 19, 18] for full details. The *wave propagation* algorithm is a Godunov type finite volume method often referred as *REA algorithm*, standing for reconstruction-evolve-average, making use of Riemann problems to determine the numerical update at each time step. Godunov's method uses the Riemann solutions to evaluate cell interface fluxes at each time step. In LeVeque's wave propagation algorithm the waves arising in Riemann solutions are re-averaged onto adjacent grid cells in order to update the numerical solution [15]. LeVeque's method is applicable to hyperbolic systems of the form (2.2). The solution to the Riemann problem consists of m waves denoted by $\mathcal{W}^p \in \mathbb{R}^m$ propagating out from each grid cell interface at speeds s^p. These waves are related to the jump discontinuity at each grid cell interface via

$$\mathrm{Q}_i - \mathrm{Q}_{i-1} = \sum_{p=1}^{m} \mathcal{W}^p_{i-1/2} = \sum_{p=1}^{m} \alpha^p_{i-1/2} r^p_{i-1/2}\,, \tag{3.1}$$

where $r^p_{i-1/2}$ are eigenvectors of the approximate flux Jacobian $\widehat{A}_{i-1/2}$ and $\mathrm{Q}^n_i = \frac{1}{\Delta x}\int_{\mathcal{C}_i} \mathfrak{q}\,(x, t^n)\,dx$ with $\mathcal{C}_i = [x_{i-1/2}, x_{i+1/2}]$, $\Delta x = x_{i+1/2} - x_{i-1/2}$ and $\Delta t = t^{n+1} - t^n$ and the domain is partitioned into grid cells $\mathcal{C}$. This amounts to a projection of the jump in Q onto the eigenspace of $\widehat{A}_{i-1/2}$. The first order upwind method then reads

$$\mathrm{Q}^{n+1}_i = \mathrm{Q}^n_i - \frac{\Delta t}{\Delta x}\left(\mathcal{A}^+\Delta\mathrm{Q}_{i-1/2} + \mathcal{A}^-\Delta\mathrm{Q}_{i+1/2}\right)\,. \tag{3.2}$$

The fluctuations $\mathcal{A}^\pm\Delta\mathrm{Q}^n_{i\mp1/2}$ are determined by solutions to Riemann problems at the cell interfaces $x_{i\pm1/2}$. The term $\mathcal{A}^+\Delta\mathrm{Q}_{i-1/2}$ represents the net updating contribution from the rightward moving waves into grid cell $\mathcal{C}_i$ from the left interface, and $\mathcal{A}^-\Delta\mathrm{Q}_{i+1/2}$ represents the net updating contribution from the leftward moving waves into cell $\mathcal{C}_i$ from the right interface. These fluctuations can be defined in terms of waves as

$$\mathcal{A}^\pm\Delta\mathrm{Q}_{i-1/2} = \sum_{p=1}^{m}\left(s^p_{i-1/2}\right)^\pm \mathcal{W}^p_{i-1/2}\,, \tag{3.3}$$

where $s^+_{i-1/2} = \max(s^p_{i-1/2}, 0)$ and $s^-_{i-1/2} = \min(s^p_{i-1/2}, 0)$. The wave propagation method (3.2) can be extended to second order accuracy using limiters applied to each wave such that

$$\mathrm{Q}^{n+1}_i = \mathrm{Q}^n_i - \frac{\Delta t}{\Delta x}\left(\mathcal{A}^+\Delta\mathrm{Q}_{i-1/2} + \mathcal{A}^-\Delta\mathrm{Q}_{i+1/2}\right) - \frac{\Delta t}{\Delta x}\left(\widetilde{F}_{i+1/2} - \widetilde{F}_{i-1/2}\right)\,, \tag{3.4}$$

where

$$\widetilde{F}_{i-1/2} = \tfrac{1}{2}\sum_{p=1}^{m} |s^p_{i-1/2}|\left(1 - \frac{\Delta t}{\Delta x}|s^p_{i-1/2}|\right)\widetilde{\mathcal{W}}^p_{i-1/2}\,,$$

where $\widetilde{\mathcal{W}}^p_{i-1/2}$ are limited versions of $\mathcal{W}^p_{i-1/2}$. There are different standard limiter functions that ensure TVD stability of the solution (see [23, 15]). A common choice for the pair $\{r^p_{i-1/2}, s^p_{i-1/2}\}$ is the p^{th} eigenpair of a local linear approximation to the flux Jacobian matrix $\widehat{A}(\mathsf{q})$ at $x_{i-1/2}$ such as Roe averaging. In [17] high-order wave propagation algorithms are presented for hyperbolic systems. These methods combine the notion of wave propagation [22, 23] and the method of lines and can in principle be extended to arbitrarily high order accuracy by the use of high-order accurate spatial reconstructions and high-order accurate ODE solvers [17]. The implementations presented in [17] are based on the fifth-order accurate weighted essentially non-oscillatory (WENO) reconstruction and a fourth-order accurate strong-stability-preserving Runge-Kutta scheme. This work also extends the f-wave approach (described below) to high-order WENO schemes. A study of how these high-order algorithms could be adapted for the numerical integration of two-layer shallow fluid flows inside a vessel with a rigid-lid is an interesting topic for further study.

A consistent alternative approach to the wave propagation method (3.1) for a conservation law is to decompose the jump in fluxes into waves instead of the states q such that

$$f\left(\mathrm{Q}_i\right) - f\left(\mathrm{Q}_{i-1}\right) = \sum_{p=1}^{m} \mathcal{Z}^p_{i-1/2} = \sum_{p=1}^{m} \beta^p_{i-1/2} r^p_{i-1/2}\,, \tag{3.5}$$

where the waves $\mathcal{Z}^p_{i-1/2} = \beta^p_{i-1/2} r^p_{i-1/2}$ are called *f-waves* and represent propagating jumps in the flux and similar to the $\mathcal{W}$s we have $\mathcal{Z}^p \in \mathbb{R}^m$. Fluctuations are therefore defined by

$$\mathcal{A}^{\pm}\Delta\mathrm{Q}_{i-1/2} = \sum_{p=1}^{m} \mathrm{sgn}(s^p_{i-1/2})\mathcal{Z}^p_{i-1/2}\,. \tag{3.6}$$

The higher order correction terms are given by

$$\widetilde{F}_{i-1/2} = \tfrac{1}{2}\sum_{p=1}^{m} \mathrm{sgn}(s^p_{i-1/2})\left(1 - \frac{\Delta t}{\Delta x}|s^p_{i-1/2}|\right)\widetilde{\mathcal{Z}}^p_{i-1/2}\,, \tag{3.7}$$

where $\widetilde{\mathcal{Z}}^p_{i-1/2}$ is a limited version of the f-wave $\mathcal{Z}^p_{i-1/2}$ using a TVD limiter [23].

The advantage of using the f-wave method over the wave-propagation method is that it is conservative regardless of the linearization used for the flux Jacobian to calculate the eigenspace. It also extends to spatially varying flux terms $f(\mathsf{q}, x)$. The source terms can be incorporated directly into the waves by subtracting them from the jump in the flux difference and projecting the resulting vector onto the eigenspace such that

$$\delta = f\left(\mathrm{Q}_i\right) - f\left(\mathrm{Q}_{i-1}\right) - \Delta x \Psi_{i-1/2} = \sum_{p=1}^{m} \mathcal{Z}^p_{i-1/2}\,, \tag{3.8}$$

for some representation of the source term Ψ at $x_{i-1/2}$ such that

$$\Delta x \Psi_{i-1/2} \approx \int \Psi\left(\mathsf{q}, x\right) dx\,.$$

The basic steps in implementing the f-wave-propagation method are the evaluation of the relevant states to the Riemann problem using the vectors Q_i and Q_{i-1}, computation of the eigenvalues and eigenvectors (s^p, r^p), computation of the jump in the fluxes and source terms δ, projection of δ onto the eigenspace to determine the f-waves $\mathcal{Z}^p$, and finally calculation of the fluctuations $\mathcal{A}^{\pm}\Delta\mathrm{Q}$ [27]. For most of the simulations in this paper the eigenstructure of the linearized equations is used as a basis for the approximation of the eigenvalues and eigenvectors of the nonlinear systems. See [26, 27] for more details.

4 Exact solutions of linearised equations

In this section exact solutions for the linearised version of the governing equations (1.1) are presented with no-flow and influx-efflux boundary conditions in order to validate the linear two-layer f-wave solvers. Consider the linearisation of the unforced system (1.1) about the trivial state,

$$\begin{aligned} h_1(x,t) &= h_1^0 + \widetilde{h}_1(x,t)\,, \quad h_2(x,t) = h_2^0 + \widetilde{h}_2(x,t)\,, \\ u_1(x,t) &= \widetilde{u}_1(x,t)\,, \quad u_2(x,t) = \widetilde{u}_2(x,t)\,, \quad p(x,t) = \widetilde{p}(x,t)\,. \end{aligned}$$

The linearised equations are

$$\widetilde{\mathsf{q}}_t + A(\widetilde{\mathsf{q}})\,\widetilde{\mathsf{q}}_x = \widehat{\Psi}(\widetilde{\mathsf{q}})\,, \tag{4.1}$$

where

$$\widetilde{\mathsf{q}} = \begin{bmatrix} \rho_1\widetilde{h}_1 \\ \rho_1 h_1^0\widetilde{u}_1 \\ \rho_2\widetilde{h}_2 \\ \rho_2 h_2^0\widetilde{u}_2 \end{bmatrix}, \quad A(\widetilde{\mathsf{q}}) = \begin{bmatrix} 0 & 1 & 0 & 0 \\ gh_1^0 & 0 & rgh_1^0 & 0 \\ 0 & 0 & 0 & 1 \\ gh_2^0 & 0 & gh_2^0 & 0 \end{bmatrix}, \quad \widehat{\Psi}(\widetilde{\mathsf{q}}) = \begin{bmatrix} 0 \\ -h_1^0\widetilde{p}_x \\ 0 \\ -h_2^0\widetilde{p}_x \end{bmatrix},$$

with the constraint $\widetilde{h}_1(x,t) + \widetilde{h}_2(x,t) = 0$. The eigenstructure of $A(\widetilde{\mathsf{q}})$ is given in (2.12) and (2.13). Differentiating the rigid-lid constraint equation $\widetilde{h}_1 + \widetilde{h}_2 = 0$ with respect to time and using the mass equations in (4.1) gives

$$h_1^0\widetilde{u}_1 + h_2^0\widetilde{u}_2 = Q(t)\,, \tag{4.2}$$

which is independent of x. The function $Q(t)$ is determined by the boundary conditions on the horizontal velocities. Differentiating (4.2) with respect to time and using the momentum equations in (4.1) gives an equation for the pressure gradient at the rigid-lid in terms of Q_t,

$$\frac{\partial\widetilde{p}}{\partial x} = \frac{\rho_1\rho_2}{\rho_2 h_1^0 + \rho_1 h_2^0}\left(-gh_2^0\left(\frac{\partial\widetilde{h}_2}{\partial x} + r\frac{\partial\widetilde{h}_1}{\partial x}\right) - \frac{dQ}{dt}\right). \tag{4.3}$$

Consider harmonic solutions of the linearised equations of the following form

$$\begin{aligned} \widetilde{h}_1(x,t) &= H_1(x)\cos\omega t\,, \quad \widetilde{h}_2(x,t) = H_2(x)\cos\omega t\,, \\ \widetilde{u}_1(x,t) &= A_1(x)\sin\omega t\,, \quad \widetilde{u}_2(x,t) = A_2(x)\sin\omega t\,, \\ \widetilde{p}(x,t) &= \widehat{p}(x)\cos\omega t\,. \end{aligned} \tag{4.4}$$

Substitution into the linear equations (4.1) and imposing the no-flow boundary conditions at $x = 0, L$, then gives

$$\begin{aligned} h_1(x,t) &= h_1^0 + \frac{h_1^0}{\omega} G\alpha \cos\alpha x \cos\omega t\,, \quad h_2(x,t) = h_2^0 - \frac{h_1^0}{\omega} G\alpha \cos\alpha x \cos\omega t\,, \\ u_1(x,t) &= G\sin\alpha x \sin\omega t\,, \quad u_2(x,t) = -\frac{h_1^0}{h_2^0} G\sin\alpha x \sin\omega t\,, \end{aligned} \tag{4.5}$$

with

$$\alpha = \frac{n\pi}{L}\,, \quad \omega = \frac{n\pi}{L}\sqrt{\frac{\rho_2 g' h_1^0 h_2^0}{\rho_2 h_1^0 + \rho_1 h_2^0}}\,, \tag{4.6}$$

for any integer n, and the linearised pressure field is

$$\widetilde{p}(x,t) = \frac{\rho_1 g' h_2^0}{h_1^0 + r h_2^0}\,\widetilde{h}_1(x,t) + p_0 \cos\omega t\,,$$

where p_0 is an arbitrary constant.

Harmonic solutions with *influx-efflux* boundary conditions can also be found. Starting with (4.2) and assuming that $Q(t) = \varepsilon \sin\omega t$ and considering periodic solutions of the form (4.4) we get

$$h_1^0 A_1(x) + h_2^0 A_2(x) = \varepsilon\,,$$

and equation (4.3) reduces to

$$-\left(\frac{\rho_2 h_1^0 + \rho_1 h_2^0}{\rho_1 \rho_2}\right)\widehat{p}_x + g' h_2^0 H_{1x} = \varepsilon\omega\,.$$

Combining this with the third equation of (4.1) then gives

$$\frac{d^2 A_1}{dx^2} + \gamma^2 A_1 - \frac{\varepsilon\omega^2}{g' h_1^0 h_2^0} = 0\,, \quad \gamma^2 = \frac{\omega^2(\rho_2 h_1^0 + \rho_1 h_2^0)}{\rho_2 g' h_1^0 h_2^0}\,, \tag{4.7}$$

with solution

$$A_1(x) = F\cos\gamma x + G\sin\gamma x + \frac{\varepsilon\omega^2}{\gamma^2 g' h_1^0 h_2^0}\,,$$

where F, G and ω are arbitrary constants. So the harmonic solutions with influx-efflux boundary conditions and prescribed $Q(t)$ are

$$\begin{aligned} h_1(x,t) &= h_1^0 + \frac{h_1^0}{\omega}\left(-F\gamma\sin\gamma x + G\gamma\cos\gamma x\right)\cos\omega t\,, \\ h_2(x,t) &= h_2^0 - \frac{h_1^0}{\omega}\left(-F\gamma\sin\gamma x + G\gamma\cos\gamma x\right)\cos\omega t\,, \\ u_1(x,t) &= \left(F\cos\gamma x + G\sin\gamma x + \frac{\varepsilon\omega^2}{\gamma^2 g' h_1^0 h_2^0}\right)\sin\omega t\,, \\ u_2(x,t) &= \frac{\varepsilon}{h_2^0} - \frac{h_1^0}{h_2^0}\left(F\cos\gamma x + G\sin\gamma x + \frac{\varepsilon\omega^2}{\gamma^2 g' h_1^0 h_2^0}\right)\sin\omega t\,, \end{aligned} \tag{4.8}$$

with γ and ω as given in (4.7). Further details on the derivation of the linear equations can be found in [2].

5 Numerical simulations with rigid walls at $x = 0, L$

In this section, results of the numerical simulations are presented for the case where the forcing is absent, $q(t) = 0$, and no-flow boundary conditions are imposed at the horizontal boundaries

$$u_1(0,t) = u_2(0,t) = u_1(L,t) = u_2(L,t) = 0\,. \tag{5.1}$$

First linear simulations are presented for validation, and compared to the exact linear solutions derived in §4, and then fully nonlinear solutions with initial shock wave profiles are presented. In all cases the numerical schemes are programmed in MATLAB on a Windows 7, 64-bit Operating System with Processor of Intel(R) Core(TM) i7-3940XM CPU @ 3.20 GHz with Memory of 32 GB. The typical clock time for 30000 time steps is about 6 minutes.

5.1 Linear simulations with rigid wall boundary conditions

The exact solution to the linearised equations are given in §4. The pressure gradient (4.3) in this case simplifies to

$$\frac{\partial \widetilde{p}}{\partial x} = \frac{\rho_1\rho_2}{\rho_2 h_1^0 + \rho_1 h_2^0}\left(-g h_2^0\left(\frac{\partial \widetilde{h}_2}{\partial x} + r\frac{\partial \widetilde{h}_1}{\partial x}\right)\right)\,, \tag{5.2}$$

which would be considered in the jump in the flux vectors δ in (3.8) and the resulting differences are

$$\delta \;=\; \begin{bmatrix} [\rho_1 h_1^0 \widetilde{u}_1] \\ [\rho_1 g h_1^0 \widetilde{h}_1] + [\rho_1 g h_1^0 \widetilde{h}_2] + h_1^0 \mathsf{A} \\ [\rho_2 h_2^0 \widetilde{u}_2] \\ [\rho_2 g h_2^0 \widetilde{h}_2 + \rho_1 g h_1^0 \widetilde{h}_2 + \rho_1 g h_2^0 \widetilde{h}_1] - [\rho_1 g h_1^0 \widetilde{h}_2] + h_2^0 \mathsf{A} \end{bmatrix}\,, \tag{5.3}$$

where [.] represents the state differences across the cell interface and

$$\mathsf{A} \;=\; \frac{\rho_1\rho_2}{\rho_2 h_1^0 + \rho_1 h_2^0}\left(-g h_2^0 [\widetilde{h}_2 + r\widetilde{h}_1]\right)\,.$$

Before presenting some numerical results the required steps in implementing the f-wave-propagation numerical algorithms for the linear and nonlinear two-layer shallow interfacial equations are summarized as follows:

1. Determination of the unknown variables h_1, u_1, h_2 and u_2 at time level n on the left and right sides of each grid cell interface.
2. Computation of the eigenvalues and eigenvectors (s^p, r^p) for the internal and external waves based on (2.12) and (2.13) but using the full values of β, h_1 and h_2 for the nonlinear equations.
3. Computation of the jump in the fluxes and source terms δ which is defined in (5.3) and (5.6) for the linear and nonlinear equations, respectively.

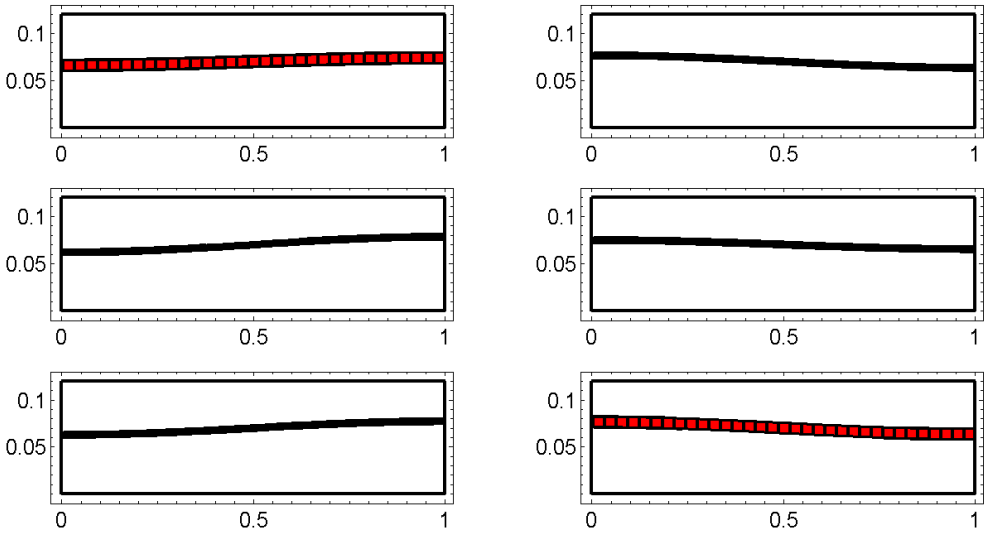

Figure 2: Snapshots of the wave profile at $t = 2\,s$, $t = 7\,s$ for the first row from left to right, $t = 12\,s$, $t = 19\,s$ for the second row from left to right, and $t = 24\,s$, $t = 30\,s$ for the third row from left to right. The horizontal axis is $x\,(m)$ and the vertical axis is the interface height $h(x,t)$. The numerical solution is shown in solid line and the exact solution in dashed red line.

4. Projection of the jump vector δ onto the eigenspaces in order to determine the f-waves $\mathcal{Z}^p$.

5. Splitting each f-wave into two waves if it is expected to be an entropy violating transonic rarefaction wave (see [24]).

6. Calculation of the fluctuations $\mathcal{A}^{\pm}\Delta \mathrm{Q}_{i-1/2}$ using (3.6) and the higher order correction terms $\widetilde{F}_{i-1/2}$ using (3.7).

7. Calculation of the state vector Q_i at time level $n+1$ using (3.4).

8. Updating the state vector Q_i for problems with time-dependent source terms by solving the ODEs (6.2) for the two-layer shallow interfacial sloshing problem with prescribed surge forcing and by solving the ODEs (7.4) for the two-layer problem with open boundary conditions.

The first simulation is a comparison with the exact oscillatory solution (4.5) using the second order (in time and space) scheme (3.4) which is run in double precision. Take the input parameters as

$$G = .03\,m\,, \quad n = 1\,, \quad \rho_1 = 900\,kg/m^3\,, \quad \rho_2 = 1000\,kg/m^3\,, \quad L = 1\,m\,,$$

$$h_1^0 = .05\,m\,, \quad h_2^0 = .07\,m\,, \quad \Delta x = .01\,m\,, \quad \Delta t = .001\,sec\,, \quad g = 9.81\,m/sec^2\,.$$

Figure 2 shows the snapshots of the computed and exact wave profiles up to $30\,sec$. The numerical solutions are in good agreement with the exact solutions. For the simulations with rigid wall boundary condition the constraint equation (4.2) modifies to

$$h_1^0\widetilde{u}_1 + h_2^0\widetilde{u}_2 = 0\,.$$

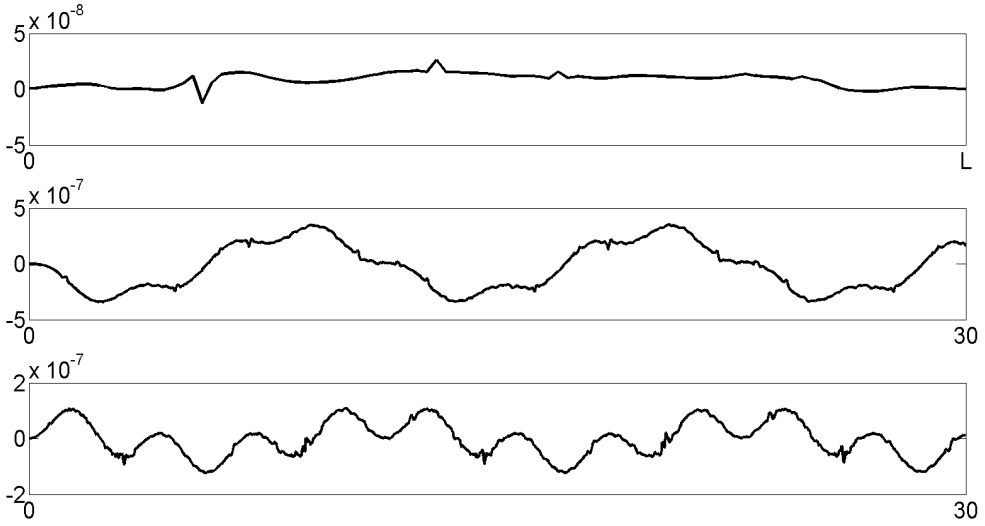

Figure 3: First row: $h_1^0\widetilde{u}_1 + h_2^0\widetilde{u}_2$ at $t = 10sec$. Second row: $\widetilde{h}_1 + \widetilde{h}_2$ at $x = .2m$ versus time. Third row: $h_1^0\widetilde{u}_1 + h_2^0\widetilde{u}_2$ at $x = .5m$ versus time.

Denoting the interior values of the cell averages by $\mathrm{Q}_1^n, \ldots, \mathrm{Q}_N^n$ then the ghost cell values for the simulations with no-flow boundary conditions are $\mathrm{Q}_0^{1-3,n} = \mathrm{Q}_1^{1-3,n}$, $\mathrm{Q}_{-1}^{1-3,n} = \mathrm{Q}_2^{1-3,n}$, $\mathrm{Q}_{N+1}^{1-3,n} = \mathrm{Q}_N^{1-3,n}$, $\mathrm{Q}_{N+2}^{1-3,n} = \mathrm{Q}_{N-1}^{1-3,n}$, $\mathrm{Q}_0^{2-4,n} = -\mathrm{Q}_1^{2-4,n}$, $\mathrm{Q}_{-1}^{2-4,n} = -\mathrm{Q}_2^{2-4,n}$, $\mathrm{Q}_{N+1}^{2-4,n} = -\mathrm{Q}_N^{2-4,n}$, and $\mathrm{Q}_{N+2}^{2-4,n} = -\mathrm{Q}_{N-1}^{2-4,n}$ where $\mathrm{Q}_0^{1-3,n}$ are the first and third components of the vector Q_0^n, and $\mathrm{Q}_0^{2-4,n}$ are the second and fourth components of the vector Q_0^n. Injecting these values for the ghost cells would result in no-flow boundary conditions for the rigid walls. Numerical errors in preservation of the two constraints are shown in Figure 3. The first row in Figure 3 shows $h_1^0\widetilde{u}_1 + h_2^0\widetilde{u}_2$ at $t = 30sec$, the second row shows the conservation of the rigid-lid constraint $\widetilde{h}_1 + \widetilde{h}_2 = 0$ at $x = .2m$ versus time and the third row shows $h_1^0\widetilde{u}_1 + h_2^0\widetilde{u}_2 = 0$ at $x = .5m$ versus time. The system constraints are locally preserved with an error of order 10^{-7}. Our observation shows that the errors remain bounded after 3×10^4 time steps.

The magnitude of the error between the exact and numerical solutions can be quantified by using the L^1 norm. The L^1 norm is commonly used for conservation laws [23]. Denoting the numerical solution for the linear system (4.1) in each grid cell on space-time grid by Q_i^n and the exact solution by $\widetilde{\mathsf{q}}_i^n = \frac{1}{\Delta x}\int_{x_{i-1/2}}^{x_{i+1/2}} \widetilde{\mathsf{q}}\,(x, t^n)\,dx$, the *global error* at time $T = \mathcal{N}\Delta t$ is (see [23])

$$\mathcal{E}_i^{\mathcal{N}} = \mathrm{Q}_i^{\mathcal{N}} - \widetilde{\mathsf{q}}_i^{\mathcal{N}},$$

and the L^1 norm is

$$\|\mathcal{E}^{\mathcal{N}}\| = \Delta x \sum_{i=1}^{N} |\mathcal{E}_i^{\mathcal{N}}|.$$

The L^1 errors in the numerical solutions versus time are shown in Figure 4, which are the sum of the spatial and numerical errors in the numerical computations here. The error between the exact and numerical solutions for $\widetilde{h}_1$ is depicted by the black line, for $\widetilde{u}_1$ by the blue line, for $\widetilde{h}_2$ by the red line, and for $\widetilde{u}_2$ by the green line. The mesh sizes in measuring

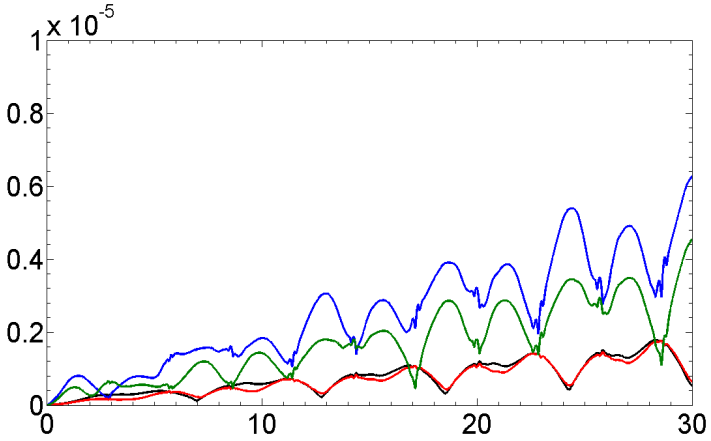

Figure 4: L^1 errors in the numerical solutions versus time for $\widetilde{h}_1$ the black line, for $\widetilde{u}_1$ the blue line, for $\widetilde{h}_2$ the red line, and for $\widetilde{u}_2$ the green line. The horizontal axis is time and the vertical axis is the L^1 error.

the errors are $\Delta t = .001\,sec$ and $\Delta x = .0033\,m$. The L^1 errors are to the order of 10^{-6} after 3×10^4 time steps.

Although the L^1 errors are slightly growing over time (as is expected and tolerable) but our numerical tests show that the errors would become smaller by decreasing the mesh sizes, and Figure 5 shows that the numerical and exact solutions for the interface profile are in very good agreement after $150\,sec$ even for a bigger spatial mesh size $\Delta x = .02\,m$. Also the errors in preserving the system constraints are to the order of 10^{-7} and remain bounded for $150\,sec$ as shown in the second and the third rows in Figure 5.

A range of other example simulations for linear rigid lid are presented in the report [2].

5.2 Nonlinear simulations with rigid wall boundary conditions

In this section the f-wave method is used to solve the nonlinear system (1.1) without the forcing terms in the momentum equations. Differentiating the constraint equation $h_1(x,t) + h_2(x,t) = d$ with respect to time and using the mass equations in (1.1) gives

$$h_1(x,t)\,u_1(x,t) + h_2(x,t)\,u_2(x,t) \;=\; Q(t)\;, \tag{5.4}$$

where $Q(t)$ is to be set by the boundary conditions. For simulations with the rigid wall boundary conditions it is zero. Differentiating this equation once more with respect to time and using the momentum equations in (1.1) gives a nonlinear equation for the pressure gradient at the rigid-lid

$$p_x \;=\; \frac{\rho_1\rho_2}{\rho_2 h_1 + \rho_1 h_2}\left(-\left(h_1u_1^2 + \tfrac{1}{2}gh_1^2 + h_2u_2^2 + \tfrac{1}{2}gh_2^2 + rgh_1h_2\right)_x - g'h_1h_{2x} - Q_t\right)\;. \tag{5.5}$$

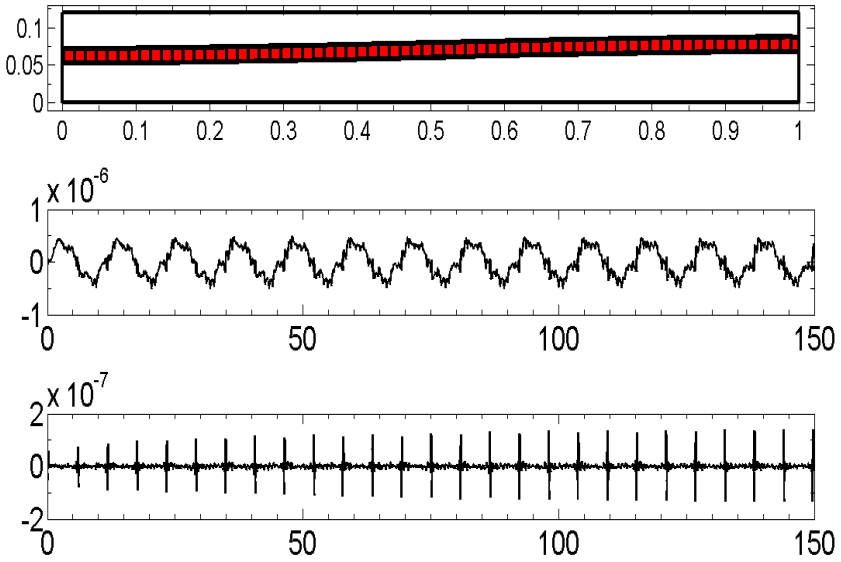

Figure 5: First row: the numerical solution against the exact solution for the interface profile at $t = 150\,s$. The exact solution is shown in dashed red line. Second row: $\widetilde{h}_1 + \widetilde{h}_2$ at $x = .5m$ versus time. Third row: $h_1^0 \widetilde{u}_1 + h_2^0 \widetilde{u}_2$ at $x = .5m$ versus time.

The jump in the flux vectors δ can computed as

$$\delta \;=\; \begin{bmatrix} [\rho_1 h_1 u_1] \\ [\rho_1 h_1 u_1^2 + \frac{1}{2}\rho_1 g h_1^2] + \rho_1 g \overline{h}_1 [h_2] + \overline{h}_1 \mathsf{B} \\ [\rho_2 h_2 u_2] \\ [\rho_2 h_2 u_2^2 + \frac{1}{2}\rho_2 g h_2^2 + \rho_1 g h_1 h_2] - \rho_1 g \overline{h}_1 [h_2] + \overline{h}_2 \mathsf{B} \end{bmatrix}, \tag{5.6}$$

with

$$\mathsf{B} \;=\; \frac{\rho_1 \rho_2}{\rho_2 \overline{h}_1 + \rho_1 \overline{h}_2} \left(-[h_1 u_1^2 + \tfrac{1}{2} g h_1^2 + h_2 u_2^2 + \tfrac{1}{2} g h_2^2 + r g h_1 h_2] - g' \overline{h}_1 [h_2] \right),$$

where $[.]$ and $\bar{.}$ represents the difference and average across the cell interface, respectively. Averages are used for layer depths as motivated by the path-conservative jump conditions assuming a linear path through state space (see [26, 27]).

For the first simulation set the initial interface a shock wave with the following form,

$$\begin{aligned} h_1(x,0) &= .07\,m\,, \quad h_2(x,0) = .05\,m \quad \text{for} \quad 0 \le x < .5\,, \\ h_1(x,0) &= .05\,m\,, \quad h_2(x,0) = .07\,m \quad \text{for} \quad .5 \le x \le 1\,, \end{aligned}$$

and fluids are taken to be quiescent at $t = 0$. Take the input parameters as

$$\begin{aligned} \rho_1 &= 900\,kg/m^3\,, \quad \rho_2 = 1000\,kg/m^3\,, \quad L = 1\,m\,, \\ \Delta x &= .01\,m\,, \quad \Delta t = .001\,sec\,, \quad g = 9.81\,m/sec^2\,. \end{aligned}$$

Figure 6 shows the snapshots of the computed wave profiles at different times. The non-linear numerical solutions are validated against a Roe-type f-wave finite volume solver

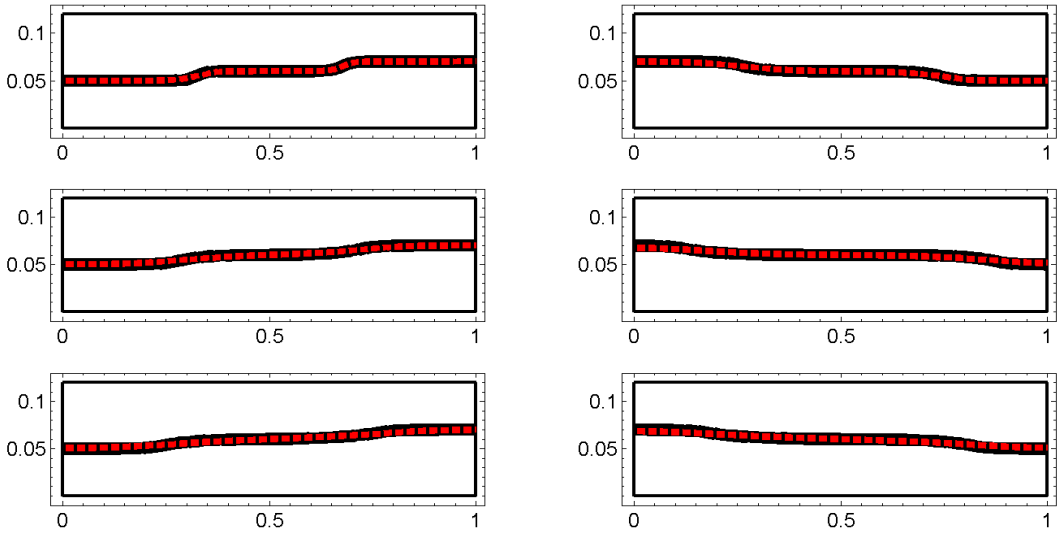

Figure 6: Snapshots of the wave profile at $t = 1\,s$, $t = 7\,s$ for the first row from left to right, $t = 12.5\,s$, $t = 19\,s$ for the second row from left to right, and $t = 24\,s$, $t = 30\,s$ for the third row from left to right. The horizontal axis is $x\,(m)$ and the vertical axis is the interface height $h(x,t)$. Numerical solutions of the Roe-type f-wave finite volume solver of [3] are depicted in dashed red line.

which is developed in [3] for the two-layer shallow interfacial sloshing equations derived by Boonkasame and Milewski (2011). Figure 6 shows that the nonlinear solutions of the presented solver are in good agreement with the numerical solutions resulted from the Roe-type f-wave solver of [3]. See [3] for details of the new Roe-type f-wave finite volume solver.

To test the ability of the numerical scheme to preserve the constraints, the error in $h_1u_1 + h_2u_2$ at $t = 30sec$ is shown in the first row in Figure 7. The second row shows the error in $h_1 + h_2 - d$ at $x = .5m$ versus time and the third row shows $h_1u_1 + h_2u_2$ at $x = .5m$ versus time. The error in preserving the rigid-lid constraint at $x = .5\,m$ is to the order of 10^{-4}, and the error in preserving the volume flux is to the order of 10^{-5}. Our observation shows that the errors remain bounded after 3×10^4 time steps.

A second simulation is shown in figure 8. The initial conditions and input data are the same as the previous run except that ρ_1 is set to $800kg/m^3$. The computed wave profiles and the numerical errors are shown in Figures 8 and 9, respectively. Numerical errors remain bounded after 3×10^4 time steps.

Additional simulations for differing density ratios and initial data are reported in [2].

6 Two-layer sloshing due to prescribed surge forcing

In this section the numerical scheme is adapted to solve the two-layer shallow-water sloshing equations in a container with a rigid-lid with prescribed surge forcing. The starting point is

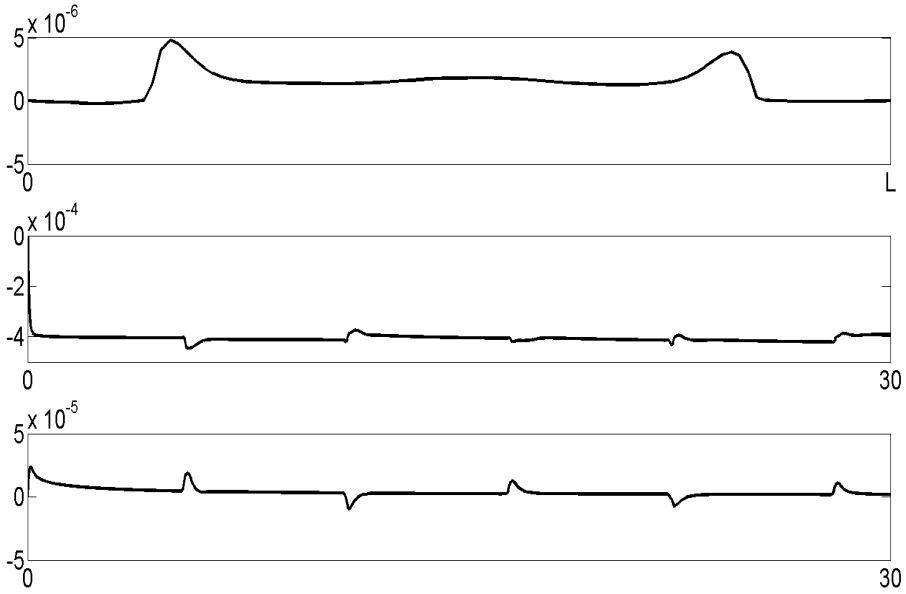

Figure 7: First row: $h_1u_1 + h_2u_2$ at $t = 30sec$. Second row: $h_1 + h_2 - d$ at $x = .5m$ versus time. Third row: $h_1u_1 + h_2u_2$ at $x = .5m$ versus time.

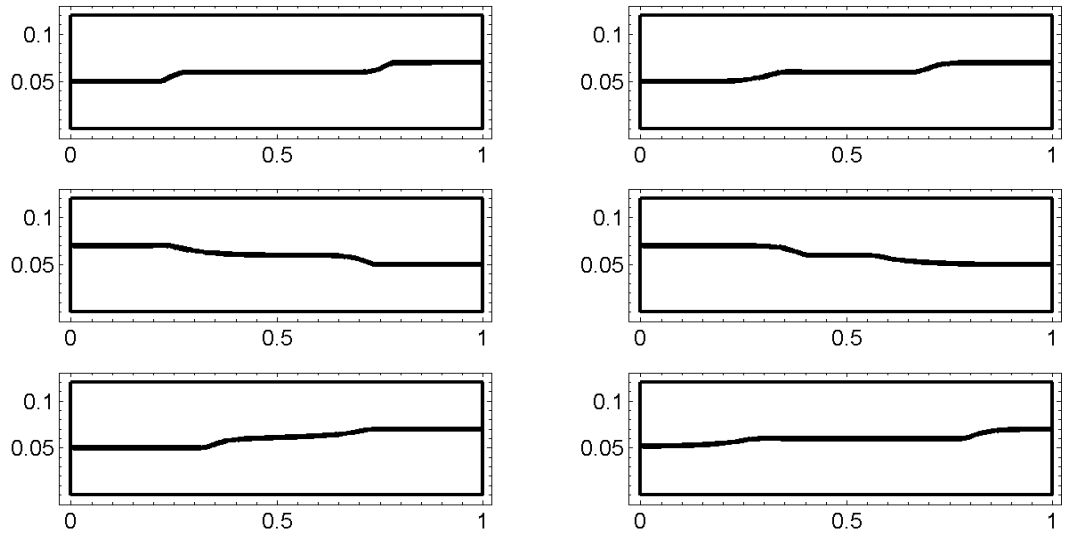

Figure 8: Nonlinear results with rigid wall boundary conditions for two fluids of densities $\rho_1 = 800\,kg/m^3$ and $\rho_2 = 1000\,kg/m^3$. Snapshots of the wave profile at $t = 1\,s$, $t = 7\,s$ for the first row from left to right, $t = 12.5\,s$, $t = 19\,s$ for the second row from left to right, and $t = 24\,s$, $t = 30\,s$ for the third row from left to right. The horizontal axis is $x\,(m)$ and the vertical axis is the interface height $h(x,t)$.

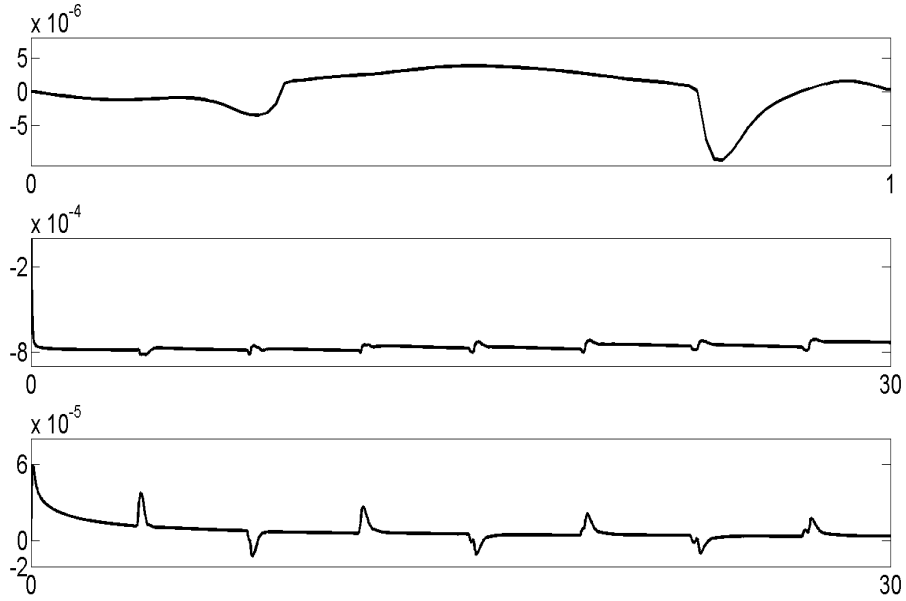

Figure 9: First row: $h_1u_1 + h_2u_2$ at $t = 30sec$. Second row: $h_1 + h_2 - d$ at $x = .5m$ versus time. Third row: $h_1u_1 + h_2u_2$ at $x = .5m$ versus time.

the governing hyperbolic system (1.1) with $q(t) \neq 0$. The boundary conditions at the vessel ends are the no flow conditions (5.1).

Differentiating the constraint equation $h_1(x,t) + h_2(x,t) = d$ twice with respect to time and using the mass and momentum equations in (1.1) gives the following equation for the pressure gradient at the rigid-lid,

$$p_x = \frac{\rho_1\rho_2}{\rho_2 h_1 + \rho_1 h_2}\left(-\left(h_1u_1^2 + \tfrac{1}{2}gh_1^2 + h_2u_2^2 + \tfrac{1}{2}gh_2^2 + rgh_1h_2\right)_x - g'h_1h_{2x} - d\ddot{q} - Q_t\right), \tag{6.1}$$

where $Q_t = 0$ with the rigid wall boundary conditions. The idea is to treat the pressure gradient the same as in the previous sections and use a fractional step approach for the $\ddot{q}$ term in (6.1) and the explicit time dependent terms in the momentum equations in (1.1). The jump in the flux vectors is computed as in (5.6). After each time step of the hyperbolic problem a time step is taken in which the momentum equations are adjusted due to the prescribed horizontal acceleration. Given h_1, h_2, u_1 and u_2 at time level n, apply the f-wave-propagation finite volume method to update these over time Δt by solving the inhomogeneous hyperbolic system (1.1) without the $\ddot{q}$ terms in the momentum equations and call the new values $h_1^\star$, $h_2^\star$, $u_1^\star$ and $u_2^\star$. Then update the star values to h_1^{n+1}, h_2^{n+1},

u_1^{n+1} and u_2^{n+1} by solving the equations

$$\begin{aligned}
\frac{\partial}{\partial t}(\rho_1 h_1) &= 0\,, \\
\frac{\partial}{\partial t}(\rho_1 h_1 u_1) &= \frac{\rho_1\rho_2 h_1}{\rho_2 h_1 + \rho_1 h_2}(d\ddot{q} + Q_t) - \rho_1 h_1 \ddot{q}\,, \\
\frac{\partial}{\partial t}(\rho_2 h_2) &= 0\,, \\
\frac{\partial}{\partial t}(\rho_2 h_2 u_2) &= \frac{\rho_1\rho_2 h_2}{\rho_2 h_1 + \rho_1 h_2}(d\ddot{q} + Q_t) - \rho_2 h_2 \ddot{q}\,.
\end{aligned} \tag{6.2}$$

For the first simulation take the initial conditions as

$$\begin{aligned}
h_1(x,0) &= .07\,m\,, \quad h_2(x,0) = .05\,m \quad \text{for} \quad 0 \le x < .5\,, \\
h_1(x,0) &= .06\,m\,, \quad h_2(x,0) = .06\,m \quad \text{for} \quad .5 \le x \le 1\,,
\end{aligned}$$

with the fluids taken to be quiescent at $t = 0$. The input parameters are

$$\begin{aligned}
\rho_1 &= 900\,kg/m^3\,, \quad \rho_2 = 1000\,kg/m^3\,, \quad L = 1\,m\,, \\
\Delta x &= .01\,m\,, \quad \Delta t = .001\,sec\,, \quad g = 9.81\,m/sec^2\,,
\end{aligned}$$

and take the prescribed surge forcing as $q(t) = \varepsilon \sin \omega t$ with $\varepsilon = .01$ and $\omega = .55294\,rad/sec$. Figure 10 shows the snapshots of the computed wave profiles up to $30sec$. The numerical solutions of the presented solver are compared with the Roe-type f-wave finite volume solver of [3] which is developed for the Boonkasame-Milewski two-layer shallow interfacial sloshing equations with an extra prescribed surge forcing function added into their equations. Figure 10 shows that the numerical solutions resulting from both solvers are in good agreement. The first row in Figure 11 shows $h_1u_1 + h_2u_2$ at $t = 30sec$, the second row shows the error in $h_1 + h_2 - d = 0$ at $x = .5m$ versus time which is to the order of 10^{-4}, and the third row shows the error in $h_1u_1 + h_2u_2 = 0$ at $x = .5m$ versus time which is to the order of 10^{-5}. Our observation shows that the errors remain bounded after 3×10^4 time steps.

A second simulation is shown in Figure 12. The initial conditions are

$$\begin{aligned}
h_1(x,0) &= .08\,m\,, \quad h_2(x,0) = .04\,m \quad \text{for} \quad 0 \le x < .5\,, \\
h_1(x,0) &= .06\,m\,, \quad h_2(x,0) = .06\,m \quad \text{for} \quad .5 \le x \le 1\,.
\end{aligned}$$

and the fluids are taken to be quiescent at $t = 0$. Take the input parameters as

$$\begin{aligned}
\rho_1 &= 800\,kg/m^3\,, \quad \rho_2 = 1000\,kg/m^3\,, \quad L = 1\,m\,, \\
\Delta x &= .01\,m\,, \quad \Delta t = .001\,sec\,, \quad g = 9.81\,m/sec^2\,,
\end{aligned}$$

and take the prescribed surge forcing as $q(t) = \varepsilon \sin \omega t$ with $\varepsilon = .01$ and $\omega = .4017 rad/sec$. Figure 12 shows the snapshots of the computed wave profiles up to $30sec$ which are compared with the numerical solutions of the Roe-type f-wave finite volume solver of [3]. Numerical results are in good agreement.

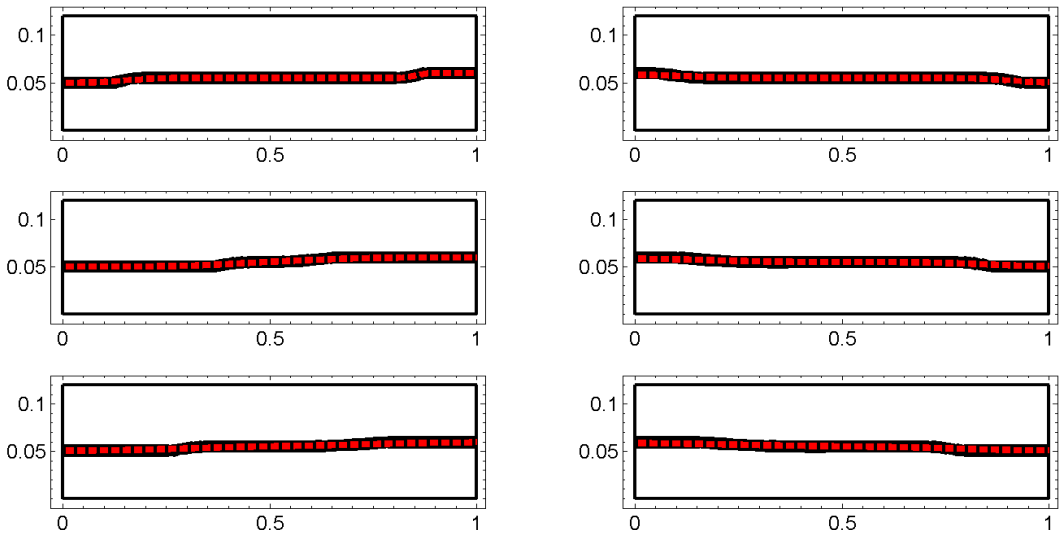

Figure 10: The interface profile for the sloshing waves with prescribed surge forcing. Snapshots of the wave profile at $t = 2\,s$, $t = 8\,s$ for the first row from left to right, $t = 12\,s$, $t = 19\,s$ for the second row from left to right, and $t = 24\,s$, $t = 30\,s$ for the third row from left to right. The horizontal axis is $x\,(m)$ and the vertical axis is the interface height $h(x,t)$. Numerical solutions of the Roe-type f-wave finite volume solver of [3] are depicted in dashed red line.

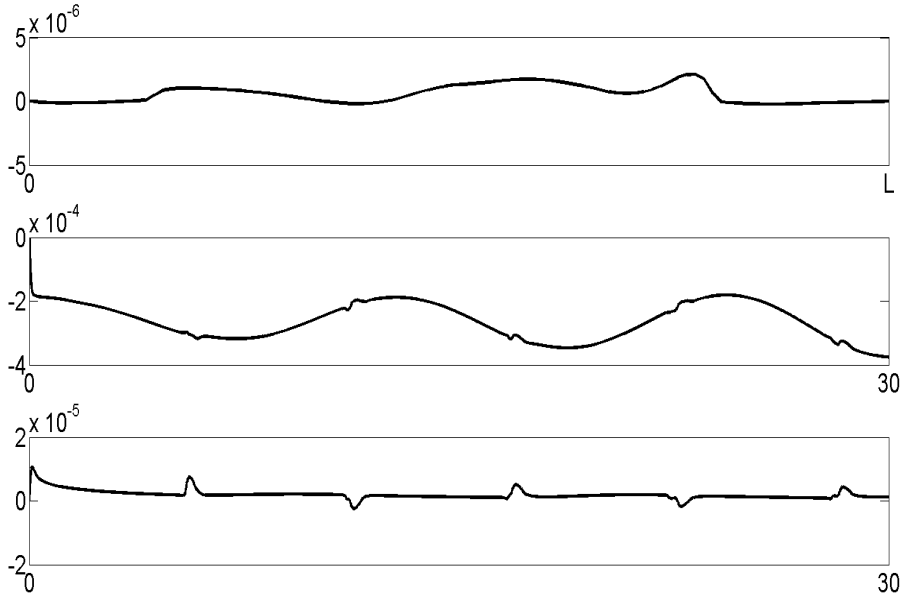

Figure 11: First row: $h_1u_1 + h_2u_2$ at $t = 30sec$. Second row: $h_1 + h_2 - d$ at $x = .5m$ versus time. Third row: $h_1u_1 + h_2u_2$ at $x = .5m$ versus time.

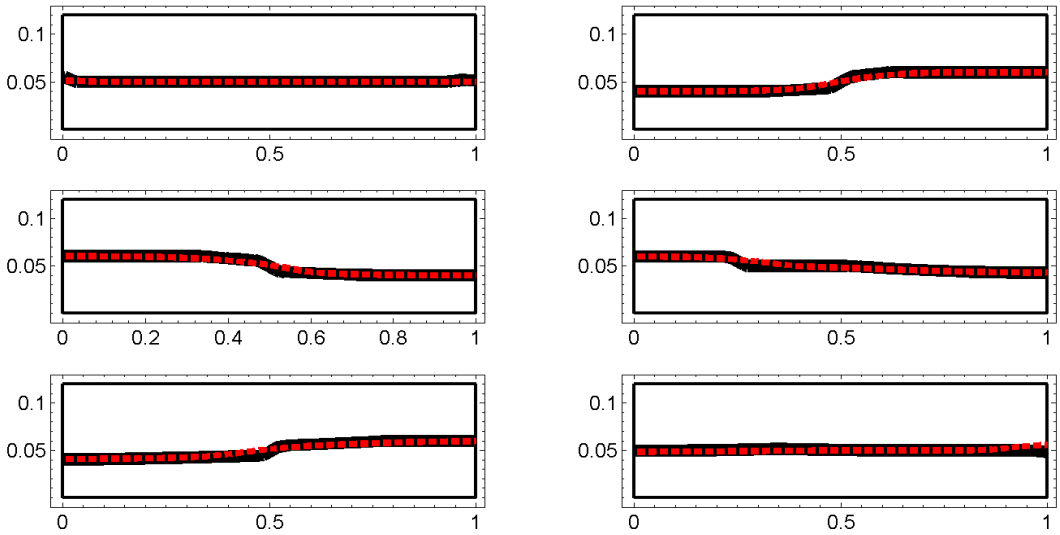

Figure 12: Sloshing shallow interfacial waves with prescribed surge forcing for two fluids of densities $\rho_1 = 800\,kg/m^3$ and $\rho_2 = 1000\,kg/m^3$. Snapshots of the wave profile at $t = 2\,s$, $t = 8\,s$ for the first row from left to right, $t = 12\,s$, $t = 19\,s$ for the second row from left to right, and $t = 24\,s$, $t = 30\,s$ for the third row from left to right. The horizontal axis is $x\,(m)$ and the vertical axis is the interface height $h(x,t)$. Numerical solutions of the Roe-type f-wave finite volume solver of [3] are depicted in dashed red line.

7 Numerical simulations with open boundary conditions at $x = 0, L$

In this section, results of the numerical simulations are presented for the case where the forcing is absent, $q(t) = 0$, and the boundaries at $x = 0, L$ are open.

First linear simulations are presented for validation, and compared to the exact linear solutions derived in §4, and then fully nonlinear solutions are presented.

7.1 Linear simulations with influx-efflux boundary conditions

For linear simulations with the influx-efflux boundary conditions, the pressure gradient (4.3) is decomposed into two parts

$$\frac{\partial \widetilde{p}}{\partial x} = \frac{\rho_1\rho_2}{\rho_2 h_1^0 + \rho_1 h_2^0}\left(-g h_2^0\left(\frac{\partial \widetilde{h}_2}{\partial x} + r\frac{\partial \widetilde{h}_1}{\partial x}\right)\right) - \frac{\rho_1\rho_2}{\rho_2 h_1^0 + \rho_1 h_2^0} Q_t\,. \tag{7.1}$$

The first part, which is the same as (5.2), would be considered in the jump in the flux vectors δ like in (5.3), and for the explicit time dependent term a fractional step approach is used such that after each time step of the hyperbolic problem a time step is taken in which the momentum equations are adjusted due to influx-efflux boundary conditions. Given $\widetilde{h}_1$, $\widetilde{h}_2$, $\widetilde{u}_1$ and $\widetilde{u}_2$ at time level n, apply the f-wave-propagation finite volume method to update

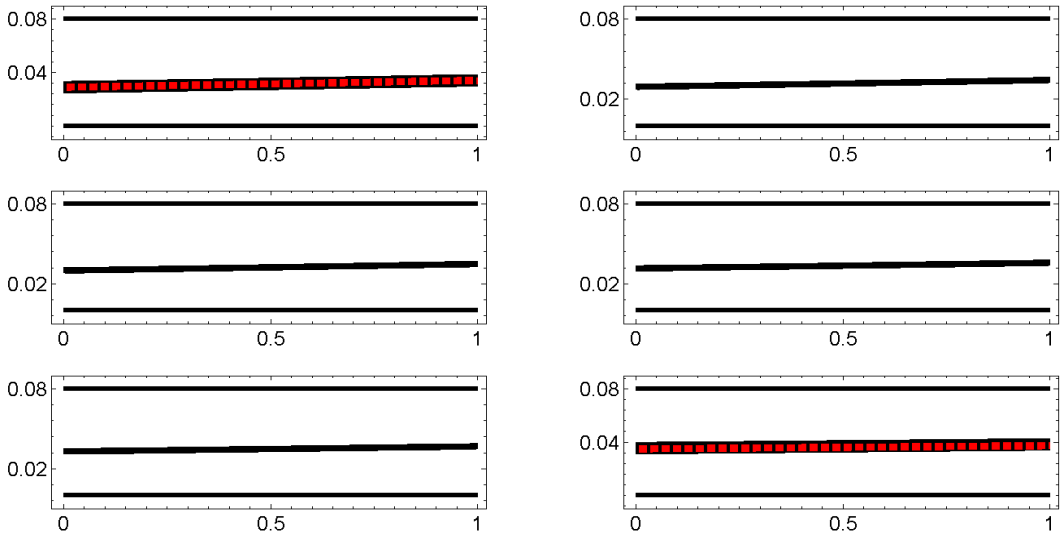

Figure 13: Snapshots of the wave profile at $t = 2\,s$, $t = 7\,s$ for the first row from left to right, $t = 12\,s$, $t = 19\,s$ for the second row from left to right, and $t = 24\,s$, $t = 30\,s$ for the third row from left to right. The horizontal axis is $x\,(m)$ and the vertical axis is the interface height $h(x,t)$. The numerical solution is shown in solid line and the exact solution in dashed red line. The top and bottom lines in each subplot represent the rigid walls.

these over time Δt by solving the inhomogeneous linear hyperbolic system (4.1) without the Q_t term in the pressure gradient and call the new values $\widetilde{h}_1^\star$, $\widetilde{h}_2^\star$, $\widetilde{u}_1^\star$ and $\widetilde{u}_2^\star$. Then update the star values to $\widetilde{h}_1^{n+1}$, $\widetilde{h}_2^{n+1}$, $\widetilde{u}_1^{n+1}$ and $\widetilde{u}_2^{n+1}$ by solving the equations

$$\begin{aligned}
\frac{\partial}{\partial t}\left(\rho_1 \widetilde{h}_1\right) &= 0\,, \\
\frac{\partial}{\partial t}\left(\rho_1 h_1^0 \widetilde{u}_1\right) &= \frac{h_1^0 \rho_1 \rho_2}{\rho_2 h_1^0 + \rho_1 h_2^0} Q_t\,, \\
\frac{\partial}{\partial t}\left(\rho_2 \widetilde{h}_2\right) &= 0\,, \\
\frac{\partial}{\partial t}\left(\rho_2 h_2^0 \widetilde{u}_2\right) &= \frac{h_2^0 \rho_1 \rho_2}{\rho_2 h_1^0 + \rho_1 h_2^0} Q_t\,.
\end{aligned} \tag{7.2}$$

The first simulation is a comparison with the exact oscillatory solution (4.8). Take the input parameters as

$$\begin{aligned}
F &= .07\,, \quad G = .04\,, \quad \omega = .03611\,rad/sec\,, \quad \rho_1 = 900\,kg/m^3\,, \quad \rho_2 = 1000\,kg/m^3\,, \\
L &= 1\,m\,, \quad h_1^0 = .04\,m\,, \quad h_2^0 = .04\,m\,, \quad \Delta x = .01\,m\,, \\
\Delta t &= .001\,sec\,, \quad g = 9.81\,m/sec^2\,, \quad \varepsilon = .005\,.
\end{aligned}$$

Figure 13 shows the snapshots of the computed and exact wave profiles at different times. The numerical and exact solutions are in good agreement. The first row in Figure 14 shows $h_1^0\widetilde{u}_1 + h_2^0\widetilde{u}_2 - Q$ at $t = 30sec$, the second row shows the errors in conservation of the rigid-lid

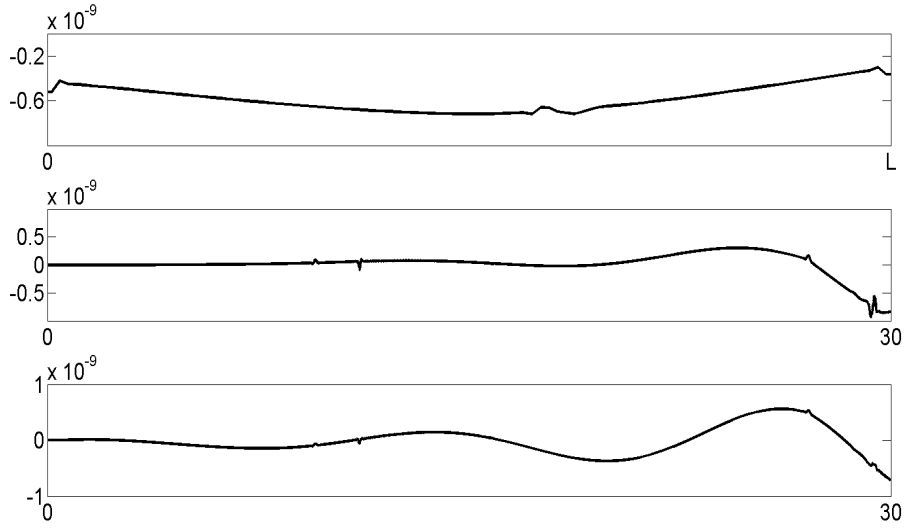

Figure 14: First row: $h_1^0\widetilde{u}_1 + h_2^0\widetilde{u}_2 - Q$ at $t = 30sec$. Second row: $\widetilde{h}_1 + \widetilde{h}_2$ at $x = .5m$ versus time. Third row: $h_1^0\widetilde{u}_1 + h_2^0\widetilde{u}_2 - Q$ at $x = .5m$ versus time.

constraint $\widetilde{h}_1 + \widetilde{h}_2 = 0$ at $x = .5m$ versus time, and the third row shows $h_1^0\widetilde{u}_1 + h_2^0\widetilde{u}_2 - Q = 0$ at $x = .5m$ versus time. Our observation shows that the numerical errors remain bounded after 3×10^4 time steps. Additional simulations are shown in the report [2].

7.2 Nonlinear simulations with influx-efflux boundary conditions

Similar to linear simulations with the influx-efflux boundary conditions, the pressure gradient (5.5) for the nonlinear calculations is decomposed into two parts

$$p_x = \frac{\rho_1\rho_2}{\rho_2 h_1 + \rho_1 h_2}\Big(-\big(h_1u_1^2 + \tfrac{1}{2}gh_1^2 + h_2u_2^2 + \tfrac{1}{2}gh_2^2 + rgh_1h_2\big)_x - g'h_1h_{2x}\Big) - \frac{\rho_1\rho_2}{\rho_2 h_1 + \rho_1 h_2}Q_t\,. \tag{7.3}$$

The first part is considered in the jump in the flux vectors δ like in (5.6), and for the explicit time dependent term a fractional step approach is used such that after each time step of the hyperbolic problem a time step is taken in which the momentum equations are adjusted due to influx-efflux boundary conditions. Given h_1^n, h_2^n, u_1^n and u_2^n at time level n, apply the f-wave-propagation finite volume method to update these over time Δt by solving the inhomogeneous nonlinear hyperbolic system (1.1) without the Q_t term in the pressure gradient and call the new values $h_1^\star$, $h_2^\star$, $u_1^\star$ and $u_2^\star$. Then update the star values to h_1^{n+1},

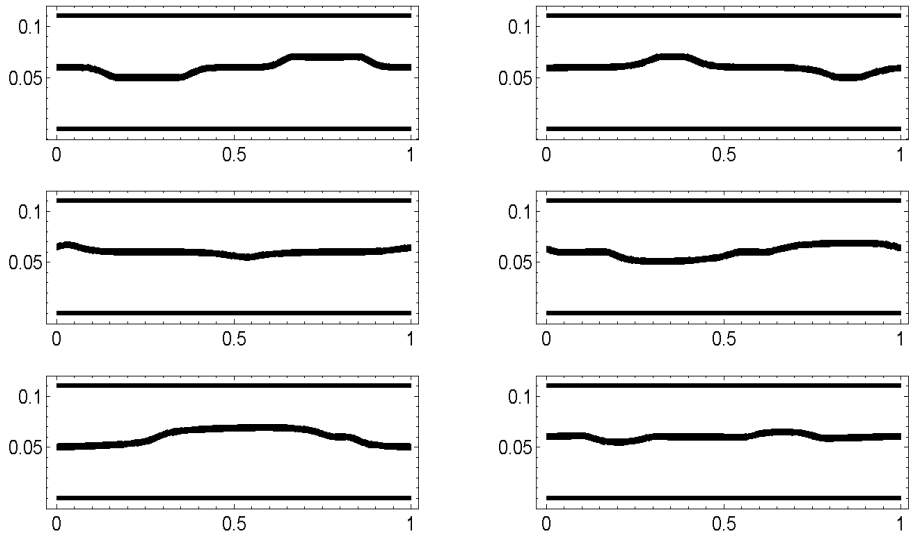

Figure 15: Snapshots of the wave profile at $t = 2\,s$, $t = 7\,s$ for the first row from left to right, $t = 12\,s$, $t = 19\,s$ for the second row from left to right, and $t = 24\,s$, $t = 30\,s$ for the third row from left to right. The horizontal axis is $x\,(m)$ and the vertical axis is the interface height $h(x,t)$. The top and bottom lines in each subplot represent the rigid walls.

h_2^{n+1}, u_1^{n+1} and u_2^{n+1} by solving the equations

$$\begin{aligned} \frac{\partial}{\partial t}(\rho_1 h_1) &= 0\,, \\ \frac{\partial}{\partial t}(\rho_1 h_1 u_1) &= \frac{\rho_1\rho_2 h_1}{\rho_2 h_1 + \rho_1 h_2} Q_t\,, \\ \frac{\partial}{\partial t}(\rho_2 h_2) &= 0\,, \\ \frac{\partial}{\partial t}(\rho_2 h_2 u_2) &= \frac{\rho_1\rho_2 h_2}{\rho_2 h_1 + \rho_1 h_2} Q_t\,. \end{aligned} \tag{7.4}$$

For the first simulation set $r = .7$ and take the initial conditions as

$$\begin{aligned} h_1(x,0) &= .04\,m\,, \quad h_2(x,0) = .07\,m \quad \text{for} \quad 0 \le x < .5\,, \\ h_1(x,0) &= .06\,m\,, \quad h_2(x,0) = .05\,m \quad \text{for} \quad .5 \le x \le 1\,. \end{aligned}$$

The fluids are taken to be quiescent at $t = 0$. Take the input parameters as

$$\begin{aligned} \rho_1 &= 700\,kg/m^3\,, \quad \rho_2 = 1000\,kg/m^3\,, \quad L = 1\,m\,, \\ \Delta x &= .01\,m\,, \quad \Delta t = .001\,sec\,, \quad g = 9.81\,m/sec^2\,, \end{aligned}$$

and set $\varepsilon = .005$ and $\omega = .0955\,rad/sec$ with periodic boundary conditions. Denoting the interior values of the cell averages by $\mathrm{Q}_1^n, \ldots, \mathrm{Q}_N^n$ then the ghost cell values are $\mathrm{Q}_0^n = \mathrm{Q}_N^n$, $\mathrm{Q}_{-1}^n = \mathrm{Q}_{N-1}^n$, $\mathrm{Q}_{N+1}^n = \mathrm{Q}_1^n$ and $\mathrm{Q}_{N+2}^n = \mathrm{Q}_2^n$. Figure 15 shows the snapshots of the computed wave profiles up to $30sec$. The first row in Figure 16 shows $h_1u_1 + h_2u_2 - Q$ at $t = 30sec$,

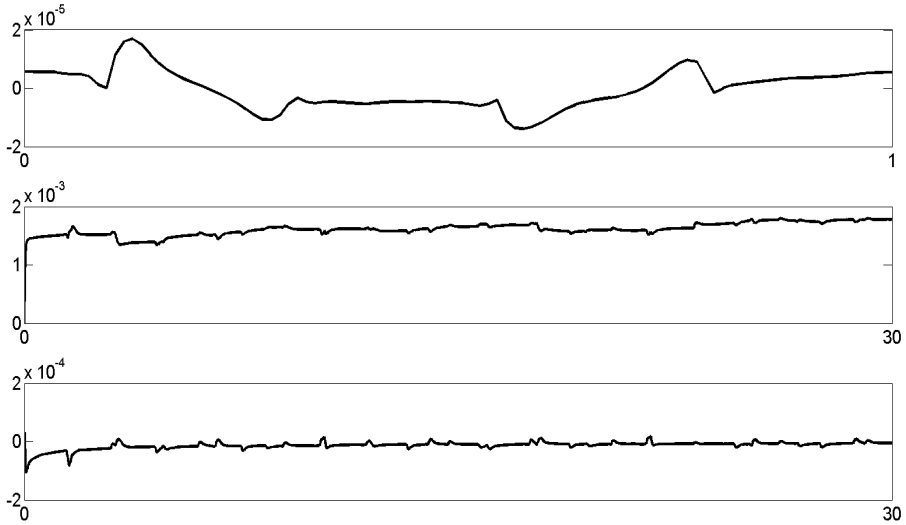

Figure 16: First row: $h_1u_1 + h_2u_2 - Q$ at $t = 30sec$. Second row: $h_1 + h_2 - d$ at $x = .5m$ versus time. Third row: $h_1u_1 + h_2u_2 - Q$ at $x = .5m$ versus time.

the second row shows the errors in $h_1 + h_2 - d = 0$ at $x = .5m$ versus time, and the third row shows $h_1u_1 + h_2u_2 - Q = 0$ at $x = .5m$ versus time. Our observation shows that the numerical errors remain bounded after 3×10^4 time steps.

A second simulation is shown in Figure 17. Take the initial conditions and input parameters the same as the previous simulation but with $\rho_1 = 600kg/m^3$. Let $Q(t) = \varepsilon \sin \omega t$ with $\varepsilon = .005$ and $\omega = .1149\, rad/sec$, and consider the boundary conditions to be periodic. Figure 17 shows snapshots of the computed wave profiles up to $30sec$.

8 Concluding remarks

The paper is devoted to the application of the high-resolution f-wave-propagation finite volume methods to the problem of two-layer inviscid, incompressible and immiscible shallow-water flows in a moving vessel with a rigid-lid. The main novel feature of the methods presented in this paper is the inclusion of the exact expression for the pressure gradient at the rigid-lid into the numerical calculations. This is done by considering the pressure gradient as a source term which is included in the jump within the flux vectors before decomposing the differences into waves propagating out from each grid cell interface. The pressure gradient is related to the volume flux that is set by boundary conditions on the horizontal velocities. The time dependent volume flux terms are handled via a fractional step approach. The same strategy is used to solve the two-layer shallow water sloshing waves with prescribed surge forcing function.

Since the wetting and drying phenomenon is very important in the efficiency of the ocean wave energy converters like the OWEL WEC, the way forward is to modify the current f-wave finite volume solvers to include wetting and drying at the rigid-lid. The interesting

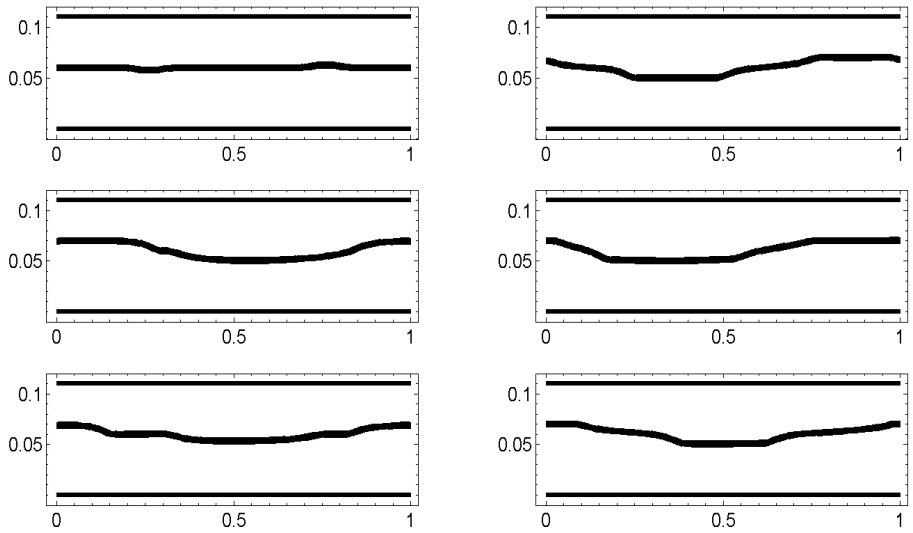

Figure 17: Snapshots of the wave profile at $t = 2\,s$, $t = 7\,s$ for the first row from left to right, $t = 12\,s$, $t = 19\,s$ for the second row from left to right, and $t = 24\,s$, $t = 30\,s$ for the third row from left to right. The horizontal axis is $x\,(m)$ and the vertical axis is the interface height $h(x,t)$. The top and bottom lines in each subplot represent the rigid walls.

point is that the volume flux which appears in the expression for the pressure gradient at the rigid-lid would play an important role in modelling the Power Take Off (PTO) system of the OWEL WEC. So the goal is to study how best to handle the time dependent source terms. One approach is to use the fractional step methods used in this paper.

Another feature of importance in WECs is the dynamic coupling between the vessel motion and the interior fluid motion. The current high-resolution f-wave finite volume solvers can be coupled to an ODE solver to study the dynamic coupling between the horizontal vehicle motion with a rigid-lid and the interior two-layer shallow-water sloshing. This coupled dynamics is discussed in [4].

Acknowledgments

The research reported in this paper is supported by the Engineering and Physical Sciences Research Council Grant EP/K008188/1. Due to confidentiality agreements with research collaborators, supporting data can only be made available to bona fide researchers subject to a non-disclosure agreement. Details of the data and how to request access are available from the University of Surrey publications repository: researchdata@surrey.ac.uk

References

[1] `http://www.owel.co.uk/`

[2] H. Alemi Ardakani. *Theory and application of f-wave finite volume methods to the two-layer shallow-water equations with a rigid-lid*, Internal Report, University of Surrey (2014).

[3] H. Alemi Ardakani. *Adaptation of f-wave finite volume methods to the Boonkasame-Milewski non-Boussinesq two-layer shallow interfacial sloshing equations coupled to the vessel motion*, Preprint (2015).

[4] H. Alemi Ardakani, T.J. Bridges & M.R. Turner. *Dynamic coupling between horizontal vessel motion and two-layer shallow-water sloshing*, Preprint (2014).

[5] R. Abgrall & S. Karni. *Two-layer shallow water systems: a relaxation approach*, SIAM J. Sci. Comput. **31** 1603–1627 (2009).

[6] P.G. Baines. *Topographic Effects in Stratified Flows*, Cambridge University Press (1995).

[7] D. Bale, R.J. LeVeque, S. Mitran & J.A. Rossmanith. *A wave propagation method for conservation laws and balance laws with spatially varying flux functions*, SIAM J. Sci. Comput. **24** 955–978 (2002).

[8] A. Boonkasame & P. Milewski. *The stability of large-amplitude shallow interfacial non-Boussinesq flows*, Stud. Appl. Math. **128** 40–58 (2011).

[9] F. Bouchut & T. Morales de Luna. *An entropy satisfying scheme for two-layer shallow water equations with uncoupled treatment*, ESAIM: M2AN **42** 683– 698 (2008).

[10] T.J. Bridges & N.M. Donaldson. *Reappraisal of criticality for two-layer flows and its role in the generation of internal solitary waves*, Phys. Fluids **19** 072111 (2007).

[11] M.J. Castro-Díaz, E.D. Fernández-Nieto, J.M. González-Vida & C. Parés-Madroñal. *Numerical treatment of the loss of hyperbolicity of the two-layer shallow-water system*, J Sci Comput **48** 16–40 (2011).

[12] M. Castro, J. Macías & C. Parés. *A Q-scheme for a class of systems of coupled conservation laws with source term. Application to a two-layer 1-D shallow water system*, ESAIM: M2AN **35** 107–127 (2001).

[13] B. Di Martino, P. Orenga, & M. Peybernes. *On a bi-layer shallow water model with rigid-lid hypothesis*, Math. Mod. Meth. Appl. Sci. **15** 843–869 (2005).

[14] D.L. George. *Finite Volume Methods and Adaptive Refinement for Tsunami Propagation and Inundation*, Ph.D. Thesis, University of Washington, Seattle, WA (2006).

[15] D.L. George. *Augmented Riemann solvers for the shallow water equations over variable topography with steady states and inundation*, J. Comp. Phys. **227** 3089–3113 (2008).

[16] Q. Jiang & R.B. Smith. *Ideal shocks in a 2-layer flow. Part I: under a rigid lid*, Tellus **53** 129–145 (2001).

[17] D.I. Ketcheson, M. Parsani & R.J. LeVeque. *High-order wave propagation algorithms for hyperbolic systems*, SIAM J. Sci. Comput. **35** A351–A377 (2013).

[18] J. Kim. *Finite Volume Methods for Tsunami Generated by Submarine Landslides*, Ph.D. Thesis, University of Washington, Seattle, WA (2014).

[19] J. Kim & R.J. LeVeque. *Two-layer shallow water system and its applications*, Proceedings of 12th International Conference on Hyperbolic Problems, College Park, Maryland (2008).

[20] M. La Rocca, G. Sciortino & M.A. Boniforti. *Interfacial gravity waves in a two-fluid system*, Fluid Dynamics Research **30** 31–66 (2002).

[21] G.A. Lawrence. *On the hydraulics of Boussinesq and non-Boussinesq two-layer flows*, J. Fluid Mech. **215** 457–480 (1990).

[22] R.J. LeVeque. *Wave propagation algorithms for multidimensional hyperbolic systems*, J. Comp. Phys. **131** 327–353 (1997).

[23] R.J. LeVeque. *Finite Volume Methods for Hyperbolic Problems, Cambridge Texts in Applied Mathematics*, Cambridge University Press, Cambridge, UK (2002).

[24] R.J. LeVeque & D.L. George. *High-Resolution Finite Volume Methods for the Shallow Water Equations with Bathymetry and Dry States*, In Advanced Numerical Models for Simulating Tsunami Waves and Runup, P. L-F. Liu, H. Yeh & C. Synolakis, editors, Advances in Coastal and Ocean Engineering, World Scientific **10** 43–73 (2007).

[25] H. Mahdizadeh, P.K. Stansby & B.D. Rogers. *On the approximation of local efflux/influx bed discharge in the shallow water equations based on a wave propagation algorithm*, Int. J. Numer. Meth. Fluids **66** 1295–1314 (2011).

[26] K.T. Mandli. *Finite Volume Methods for the Multilayer Shallow Water Equations with Applications to Storm Surge*, Ph.D. Thesis, University of Washington, Seattle, WA (2011).

[27] K.T. Mandli. *A numerical method for the two layer shallow water equations with dry states*, Ocean Modelling **72** 80–91 (2013).

[28] L.V. Ovsyannikov. *Two-layer shallow water model*, J. Appl. Mech. Tech. Phys. **20** 127–135 (1979).

[29] J.B. Schijf & J.C. Schönfled. *Theoretical considerations on the motion of salt and fresh water*, Proc. of Minn. Int. Hydraulics Conv., Joint meeting IAHR and Hyd. Div ASCE., IAHR 321–333 (1953).

[30] A.L. Stewart & P.J. Dellar. *Multilayer shallow water equations with complete Coriolis force. Part I: Derivation on a non-traditional beta-plane*, J. Fluid Mech. **690** 16–50 (2012).